Variations of stress parameters in the Southern California plate boundary around the South Central Transverse Ranges

Niloufar Abolfathian[1], Patricia Martínez-Garzón[2], Yehuda Ben-Zion[1]

[1]University of Southern California, Los Angeles, USA

[2]GFZ German Research Centre for Geosciences, Potsdam, Germany

Three key points of the research:

(1) Local stress deviations from the regional stress field provide information on dominant local loadings.

(2) Comparing stress field inversions using declustered seismicity and aftershocks help to identify the main loading in an area.

(3) Higher topography produces compressional stress components at the bottom of the seismogenic zone.

Abstract

We examine stress parameters in Southern California with a focus on the region near the South Central Transverse Ranges (SCTR), using a refined stress inversion methodology to 1981-2017 declustered and aftershocks focal mechanisms independently. Comparison between the associated stress parameters provides information on the local dominant loading. The estimated stress parameters are examined in relation to the regional stress regime and local loadings. Over the regional scale, the S_{Hmax} trends towards the NNE and the stress ratios vary from transtensional stress regime near the Eastern California Shear Zone (ECSZ), to shear stress near the SCTR, and towards transpression near the Western Transverse Ranges. Detailed analysis of stress parameters near the SCTR indicates deviations from the regional shear stress. The San Bernardino Mountain area shows S_{Hmax} direction towards NNW and transpressional stress components likely associated with the relative motion of the San Andreas Fault and ECSZ. The Cajon Pass and San Gorgonio Pass show transpressional stress regime near the bottom of the seismogenic zones likely associated with the elevated topography. In Crafton Hills, rotation of the principal stress plunges and S_{Hmax} direction and transtensional stress regime below ~10 km, along with lower estimated apparent friction coefficient suggest a weak fault possibly associated with deep creep. The results reveal effects of local loadings resolved by the performed multi-scale analysis. The study does not show significant temporal variations of stress variations near the SCTR from the average stress parameters in the analyzed 37 years.

Index Terms and Keywords

Stress, stress inversion, South Central Transverse Ranges, aftershocks, fault loading.

1. Introduction

The boundary between the North American and Pacific plates in Southern California consists of multiple active fault zones with different total offsets, slip rates and seismic activities (Figure 1). Most of the plate boundary motion and seismic hazard are associated with the San Andreas Fault (SAF) and San Jacinto Fault Zone (SJFZ). The plate boundary in the South Central Transverse Ranges (SCTR) with high topography of ~3 km associated with the San Gabriel and San Bernardino Mountains has a complex set of thrust and strike-slip faults (e.g., Matti et al., 1993; Spotila et al., 2001; Yule and Sieh, 2003), especially between Cajon Pass (CP) and San Gorgonio Pass (SGP). The Crafton Hills (CH) area between the SAF and SJFZ has significant seismicity that is relatively deep (Figure 1). Improved characterization of the stress field within and around the SCTR area can provide useful information on tectonic deformation and earthquake processes in the region. This is done in the present paper with stress inversion analyses of earthquake focal mechanisms on regional and local scales.

Previous studies examined the stress field around the SCTR and other regions in Southern California. Hardebeck and Hauksson (2001) performed stress inversion of focal mechanisms and showed that a homogeneous background stress field is not able to explain the complex faulting system and stress variations in the region. They also studied the temporal changes of stress variations in 5-year time periods between 1980 and 1999. Their results show significant changes in the orientations of the maximum horizontal compressional stress in the vicinity of major earthquakes, and no significant changes detectable within the noise level of the data related to the tectonic loading. Yang and Hauksson (2013) studied stress parameters on regional (100-500 km resolution) and local scales (less than 100km) and discussed the importance of local scale stress variations that can affect rupture zones of major M7 type earthquakes.

In the present study we use earthquake fault plane solutions from 1981 to 2017 to examine the 3D background stress field in a regional scale (Figure 1) extending from the Eastern California Shear Zone (ECSZ) to the LA basin (section 4.1), along with more detailed spatiotemporal variations of the stress field employing fault plane solutions of earthquakes from 1981 to 2017 (section 4.2). Employing a refined stress inversion methodology developed by Martínez-Garzón et al. (2016a), over larger data set compared

with previous studies, we obtain more stable stress parameters in a finer resolution of ~5 km (resolution varies with the seismicity distribution) that provide information on the local stress field and associated loadings in more detail than earlier works.

Various studies indicate that focal planes of aftershocks are in general consistent with the orientation of the major geological structures (McCloskey et al., 2003; Hardebeck, 2014). The total crustal stress field (τ_T) can be written as the sum

$$\tau_T = \tau_R + \tau_L + \Delta\tau_{ST}. \quad (1)$$

where τ_R is the regional far field loading, τ_L represents additional loading due to local features such as topography, and $\Delta\tau_{ST}$ is stress transfer from earthquakes in the considered crustal volume.

Inversions of focal mechanisms of declustered seismicity (mainshocks) provide information on the background stress field associated with the loading compoenents ($\tau_R + \tau_L$), while inversions of the aftershock mechanisms reflect the background stress field together with the internal stress transfers of the mainshocks and these events ($\tau_R + \tau_L + \Delta\tau_{ST}$). Comparing the stress fields produced by these two types of inversion can provide information on the dominant loading mechanisms of the mainshocks that drive the aftershocks. In section 4.3 we compare the estimated stress parameters from the mainshocks and the aftershocks in the focused study area around the SCTR.

2. Data and the study area

For the purpose of this study, the earthquake hypocenters are selected from the Southern California relocated catalog of Hauksson et al. (2012, extended to later years) (Figure 1) with horizontal and vertical location errors of 0.75 km and 1.25 km, respectively. The fault plane solutions are selected from the Yang et al. (2012, extended to later years) focal mechanism catalog for the total time period of 1981-2017. The selected focal mechanisms have qualities from A to D, in accordance with 5° to 55° degrees of uncertainty, where with the mentioned uncertainty range, inversions with ~40 events per grid cell, resolves a stable stress field (Martínez-Garzón et al., 2016a).

The selected focal mechanism catalog is declustered using the nearest-neighbor

proximity approach developed by Zaliapin and Ben-Zion (2013, 2020), separating the mainshock events from the aftershocks and the foreshocks. The declustered seismicity makes it possible to focus on the background tectonic stress, and separately on the stress field associated with internal stress transfers resulting the aftershocks (Martínez-Garzón et al., 2016a). The declustered events are also referred to as background seismicity.

The background hypocenters show notable variations in the selected focused area near the SCTR. The area between the main two faults of SAF and SJFZ includes 52% of all the selected background seismicity and has the deepest seismogenic thickness (defined as the depth above which 90% of the events are located) of 17.8 km (Figure 1). The background seismicity from east of the SAF comprises 34% of the selected events and displays a seismogenic thickness of 11.9 km, while the western section of the SJFZ includes 14% of the background seismicity and has a seismogenic thickness of 14.9 km. Based on the mentioned background seismicity hypocentral variations and the geological structures such as mountain ranges and the main faults we divided the area into six sub-regions (Figure 2). The sub-regions are as follows: (1) San Gabriel Mountains (SGM), (2) San Bernardino Mountains (SBM), two areas in the (3) northern and (4) eastern sections of the SBMs including parts of the ECSZ and fault system near Landers, (5) between the two main fault strands of SAF and SJFZ, and (6) Western region of the SJFZ. We separately analyze the background stress field of the mentioned sub-regions in the entire seismogenic thickness.

The stress parameters are estimated independently for the mainshocks' and aftershocks' mechanisms. Aftershocks comprise the majority of events in the SCTR (65%), while mainshocks (background events) are only 21% of the earthquakes in the selected focused study area. Should be noted that the seismogenic thickness of the mainshocks is ~16.9 km, whereas the aftershocks show a shallower seismogenic thickness of ~13.5 km in the focused study area. The ~3.4 km average hypocentral difference of the mainshocks and aftershocks is correlated with the difference in their associated main loadings. Table 1 summarizes statistical information on the distribution of the mainshocks and the aftershocks.

3. Methodology

3.1 Stress tensor inversion of focal mechanisms

In this study, we apply the refined stress inversion method developed by Martínez-Garzón et al. (2016a) on double-couple earthquake focal mechanisms Catalog in Southern California. The inversion method employs the refined MSATSI software (Martínez-Garzón et al., 2014; 2016a), which is an updated version from SATSI algorithm (Michael, 1984; Hardebeck and Michael, 2006). The assumptions of the stress inversion include: (1) The stress field is homogeneous within a considered rock volume, (2) Earthquakes occur on pre-existing faults with varying orientations, and (3) Slip on each fault occurs parallel to the direction of its tangential traction (Wallace, 1951; Bott, 1959).

The implied method includes discretizing the events based on an optimum required number of focal mechanisms per grid cell to constrain a stable stress orientation of an area (McKenzie, 1969), which in this study ~40 events is the optimum number of events per grid cell (Martínez-Garzón et al., 2016a). The study volume is discretized using the *k*-means technique (Hartigan and Wong, 1979; Martínez-Garzón et al., 2016a) into Voronoi grid cells containing the mentioned optimum number of events. The cell sizes vary in relation to seismicity density and provide estimates for the spatial resolution of the inversion (e.g. Figure 4).

The linear damped stress inversion estimates the orientations of the three principal stresses σ_1, σ_2 and σ_3 (from most to least compressive) and the stress ratio parameter, R, defined as

$$R = \frac{\sigma_1 - \sigma_2}{\sigma_1 - \sigma_3} \tag{2}$$

The stress ratio (R value) ranges between 0 and 1, with smaller and larger stress ratios in a strike-slip environment corresponding to stress regimes closer to transtensional (i.e., mixed strike-slip and normal faulting) and transpressional (i.e., mixed strike-slip and reverse faulting) fields, respectively.

The orientation of maximum horizontal compressional stress, S_{Hmax}, is computed from the orientation of the principal stress axes following Lund and Townend (2007) and the estimated trends and plunges of the principal stresses are classified into Andersonian

stress regimes: normal, strike-slip and reverse, and oblique faulting types (Zoback, 1992). Uncertainty estimations of the inversion outputs are obtained by bootstrap resampling of the original set of focal mechanisms (Michael, 1987) and provide 95% confidence intervals.

The method applies an iterative procedure to select the nodal plane that is optimally oriented for failure in the estimated stress field. During each iteration, the stress field orientation is calculated and the fault plane with the largest instability coefficient I is selected for the next iteration (Vavryčuk, 2011; 2014; Martínez-Garzón et al., 2016b). The parameter I is defined as

$$I = \frac{\tau - \mu(\sigma - 1)}{\mu + \sqrt{1 + \mu^2}}, \quad (3)$$

where μ is the apparent coefficient of friction. τ and σ are scaled shear and normal stresses, respectively. The parameter I takes values between 0 and 1, representing the least and most optimally oriented faults to failure within a given deviatoric stress field. When estimating the fault instability, a grid search is applied over values of coefficients of frictions, ranging between 0.2 and 0.8. For each grid cell, the estimated μ produces the highest overall instability coefficient (Vavryčuk, 2014). Since μ is selected based on iterative computations in the inversion procedure, we refer it as an apparent coefficient of friction.

4. Results

4.1 Regional stress variations in Southern California

Initially, we analyze the background stress distribution in a volume extending over the plate-boundary region in Southern California, from the ECSZ to the LA basin, using ~6,800 focal mechanisms from the declustered catalog between 1981-2017. To examine the 3D spatial changes of stress parameters, the selected focal mechanisms in the study area are divided into 5 km depth bins. The bin width is chosen considering the overall depth uncertainty of ~1.25 km of the resolved hypocentral locations and the optimum number of seismicity, ~40 per grid cell, in a strike-slip regime to converge to a stable stress tensor (Martínez-Garzón et al., 2016a). Focal mechanisms in each grid cell are inverted and the S_{Hmax} direction, the stress field orientations, and the stress ratio R are

estimated following the methodology discussed in section 3.

The spatial distribution of S_{Hmax} of the selected declustered seismicity over the regional scale can be divided into regions near the ECSZ, San Bernardino Mountains (SBM), the area between the SAF and SJFZ, and near the WTR (Figure 3). In the ECSZ, the S_{Hmax} is oriented toward NNE, with average azimuths of ~10º, ~15º and ~12º in the depth sections 0-5 km, 5-10 km, and 10-15 km, respectively. In the SBM, the S_{Hmax} orientation rotates towards the north and slightly NNW, with average S_{Hmax} trend of N7ºW. Between the SAF and SJFZ, S_{Hmax} generally points toward the north and NNE. In this area, near Crafton Hills, a large clockwise rotation in the S_{Hmax} direction is observed. Near the WTR and the LA basin, the S_{Hmax} directions rotate back towards NNE similar to the orientation in the ECSZ, with the difference that the WTR includes lower spatial resolution and higher uncertainty in the inferred S_{Hmax} orientation.

The stress regimes are estimated based on the relative position of the σ_1, σ_2, and σ_3 axes. The regional background stress regime is in general strike-slip with deviations near the WTR deeper than 10 km showing reverse faulting and in the ECSZ, at the 5-10 km depth section, showing oblique faulting with a mixture of strike-slip and normal faulting (Figure 3).

The variations of the estimated stress ratio *R* represent the deviation from the regional strike-slip faulting towards transtensional and transpressional stress regimes. In general, clear variations from transtension near the ECSZ to transpression near the WTR are observed at all depth ranges (Figure 4). Deviations from the regional strike-slip stress field near the SCTR include patches of higher transpressional components near CP and SGP (Figure 4c) and higher transtensional stress regimes observed near the CH (Figure 4, b to d). The CP, SGP, and CH areas are considered to display local stress components related to the local geological structures, which are discussed in more detail in the following section, 4.2.

4.2 Stress variations near the South Central Transverse Ranges

We focus on the area near the SCTR using ~3,300 focal mechanisms from the declustered catalog in the selected time period (brown box in Figure 1). We analyze the 3D variations of the stress parameters dividing the selected focal mechanisms into 5 km

depth bins and the 2D spatial variation of the stress parameters dividing the background focal mechanisms based on geological features near the SCTR.

The S_{Hmax} orientations near the SCTR are generally towards the north and NNE direction (Figure 5), with significant variation in the CH area at 15-20 km depth, where the S_{Hmax} direction rotates ~23° clockwise from the surface to the bottom of the seismogenic thickness (Abolfathian et al., 2019).

The orientations of the estimated principal stresses (shown as stereonets in Figure 5) indicate the main background stress regime of strike-slip faulting, which based on the Andersonian theory of faulting has vertical intermediate principal stress and parallel least and most compressional stress orientations with the Earth surface as the reference. The Andersonian theory for strike-slip faulting holds overall from the surface to 15 km depth in the focused study area. However, below 15 km depth, the most compressive and intermediate principal stresses' plunge angles rotates about ~30° in the CH area, and all principal stresses' plunge angles in the southern part of SGP area and close to the Hot Springs (HS) area rotate about ~15° to ~30° (Figure 5). In addition, in this depth section, the hypocenters of the selected focal mechanisms are mainly located between the two main faults of SAF and SJFZ.

Significant variations in the stress ratios are observed in the focused study area near the SCTR. In the shallowest depth bin, 0-5 km, the stress ratios follow the regional overall strike-slip faulting, varying from slightly transtensional in the most eastern section towards transpression in the most western part (Figure 4a). The same variations are observed in 5-10 km depth with amplified components of transtension and transpression in the eastern and western sections, respectively (Figure 4b). At 10-15 km depth, the higher transpressional component appears near the highest peaks of the San Bernardino Mountains near SGP, and San Gabriel Mountains close to CP (Figure 4c). At the same depth range, transtensional components emerge in the CH area. Below ~5 km, the stress ratio near the CP area changes sharply from transpression in its northwest to transtension in its southeast, even though the inversions utilized damping to smooth stress variations between the neighbor cells. The CP area is located where the SJFZ branches from the SAF and the strong change in topography exists at the edge of the San Gabriel Mountains.

The region between the SJFZ and SAF near the SCTR is highly seismically active (more than 50% of the background events in the SCTR region are between the two fault strands), and the hypocenters of the declustered seismicity are on average ~5 km deeper than the ones located outside of this region. In an effort to clarify stress variations related to fault-system interactions and topographic variations, we divide selected declustered mechanisms into six sub-regions (see section 2) and invert independently for stress parameters in each sub-regions within its entire seismogenic thickness (Figure 2). The results indicate the main faulting near the SCTR is strike-slip, with deviations including amplified reverse faulting close to the CP area and oblique/normal faulting in the ECSZ area (Figure S1). The stress ratio variations from the 6 sub-regions show the compressional components near CP and the sharp stress ratio changes between the NW and SE of the junction of the SAF and SJFZ (Figure 6), where the compressional component is likely associated with the higher topography. The transtensional stress components close to the junction could be explained in terms of the extension associated with the right-lateral strike-slip motion on the SJFZ and the nearby SAF. This region also includes sub-volumes dominated by normal faulting near CH. The areas near SGP and SBM show clear transpressional components.

The spatio-temporal variations of background stress field are also examined and found to be in general in agreement with the discussed spatial background stress field variations (Figure S2). For this purpose, we divide the entire selected declustered focal mechanisms into 5 time periods of ~8 years, namely 1981-1985, 1986-1993, 1994-2001, 2002-2009, 2010-2017, and estimate the stress parameters independently. The estimated stress parameters do not show any significant changes within these time periods.

4.3 Stress variations in the SCTR — aftershocks and depth dependency

In the last part, we compare the background stress variations with results obtained from the inversion of aftershocks mechanisms. The focused study area near the SCTR has ~3,300 focal mechanisms from the declustered catalog, while ~9,600 aftershock mechanisms are available in the selected area within the same time period. We divide the aftershock mechanisms in 5 km depth bins as applied on the background seismicity and invert for their stress parameters (Figure 7).

309 The transtensional component of background stress near the CH area is amplified
310 between ~5 to 15 km depth in the stress field inverted from the aftershocks. The
311 transpressional stress components near the SGP are also amplified in the results obtained
312 from the aftershock mechanisms, with the difference that the areas with transpressional
313 stress fields are located shallower compared with the ones obtained from the mainshocks.
314 The aftershocks show the overall thinner seismogenic thickness and amplified shallower
315 transtensional and transpressional stress components in the CH and SGP areas,
316 respectively. In contrast, no evidence of the transpressional stress components near the
317 CP area is observed in the aftershock results. Considering that in the CP area comprises
318 sparse aftershock distribution, we might not have enough resolution to resolve properly
319 the stress field from the aftershocks. The comparison of the estimated stress field from
320 the background declustered seismicity and aftershocks help to understand the main
321 loading in the selected area that reflect local loadings, as discussed below.
322
323 **5. Discussion**
324 We examine spatio-temporal variations of the stress field in the plate-boundary
325 region around the SCTR based on inversions of earthquake focal mechanisms, and
326 attempt to interpret the results in relation to different loadings, fault properties,
327 topography, and crustal depth. The primary analyzed data is a declustered catalog of the
328 focal mechanisms of Southern California earthquakes from 1981 to 2017, and is used to
329 derive the background stress fields in different scales of space and time. We also invert
330 separately focal mechanisms of aftershocks that are generally triggered by stress transfers
331 from the mainshocks. Comparisons between inversion results based on the declustered
332 seismicity and aftershocks allow us to infer dominant local loading mechanisms that exist
333 in different crustal volumes in addition to the large-scale tectonic loading.
334 On a regional scale, the background stress fields inverted from the declustered
335 catalog (Figures 3 and 4) are generally consistent with previous studies, showing
336 transtensional stress regime in the ECSZ moving towards strike-slip regime near the
337 SCTR and further transpressional stress regime in the WTR and LA basin (Hardebeck
338 and Hauksson, 2001; Yang and Hauksson, 2013). The S_{Hmax} trends show NNE direction
339 near the ECSZ and the WTR (Figure 3) in agreement with the regional S_{Hmax} directions in

Southern California (Yang and Hauksson, 2013). Various sub-volumes with clear transpressional and transtensional stress components near the SBM, CH, SGP, and CP in the SCTR do not follow the expected regional strike-slip loading and indicate additional loadings associated with local structures.

The stress inversion results based on the declustered catalog in the SBM show an average S_{Hmax} trend of N7ºW (Figure S1). Yang and Hauksson (2013) estimated S_{Hmax} variations towards the NNW in this area and presented a schematic model of the ECSZ and SAF movements near the CP, with a wedge-shaped area of SBM having counter clock-wise loading. This scenario can induce compressional stress components near SBM that are observed ($R \sim 0.6$) in the inversion results of this study (Figure 6). However, the stress field estimated from the aftershocks does not show the NNW rotation of the S_{Hmax} direction and the transpressional stress components, indicating that the proposed loading in the SBM accounts only for a small fraction of the total background loading in this area.

Previous observations indicated tensional stress near the CH area (Hardebeck and Hauksson, 2001; Yang and Hauksson, 2013; Abolfathian et al., 2019). Several studies connected the deeper seismicity and increase of normal faulting in the northern SJFZ with deep creeping below the seismogenic fault (Wdowinski, 2009; Cooke and Beyer, 2018). Our inversion results based on the declustered mechanisms are consistent with these inferences. The results of the background stress field provide the following lines of evidence that the SJFZ is weak near the bottom of the seismogenic zone in the CH area: (1) The inversion results indicate that the S_{Hmax} of the background stress field rotates clock-wise below 10 km depth, with maximum rotation at 15 km where the S_{Hmax} trend is almost perpendicular to the main surface fault trace. (2) The estimated apparent coefficient of friction indicates a weak zone with an average μ of ~0.4 below 10 km depth compared to an average value of ~0.55 in the focused study area (brown box in Figure 1) (Abolfathian et al., 2019). (3) The maximum and intermediate principal stress plunges rotate more than 45º below ~12 km depth (Abolfathian et al., 2019).

The stress inversions of aftershocks' mechanisms indicate transtensional $0<R<0.2$ stress components in the CH area (Figure 7). The aftershock results are consistent with the local background stress field estimated for the CH area rather than the regional strike-slip stress field. This suggests that the dominant loading in the CH area is associated with

a local structure that may be associated, as suggested in previous studies, with creep below the seismogenic fault. Evidence for a wide damage zone below 10 km in this area (Ben-Zion and Zaliapin, 2019) suggests that the deep creep may be associated with a wide shear zone rather than aseismic slip on a fault interface.

In the SCTR region, the SAF is associated with significant bending of the main fault by about ~20º-30º and elevated terrain. The fault bending and topography are associated with perturbations in the intermediate (vertical) stress on the non-optimally oriented fault (dipping fault) at seismogenic depth (Fialko et al., 2005). The CP and SGP areas located near elevated topography in the SCTR are associated with transpression stress fields. In the SGP area, the strike-slip faulting regime is dominant from the surface to 10 km depth, while transpressional stress components are significant below 10 km. The same stress pattern exists in the CP area, with significant transpressional stress components below ~5 km (Figure 4). The observed transpressional stress fields imply that the parts of the SAF passing through the SGP and CP may be dipping within the seismogenic depth. This is consistent with seismological observations of Fuis et al. (2012) and others.

The stress field estimated from the aftershock mechanisms in the SGP indicates higher compressional, $0.8<R<1$, stress components (Figure 7) and is in agreement with the loading from the topography rather than the regional strike-slip stress field, suggesting that the dominant stress field near SGP is associated with the topography (e.g., Fialko et al., 2005). In contrast, no evidence of compressional stress components is observed in the stress field inverted from the aftershock mechanisms near CP; this may be due to the fewer available aftershock mechanisms in this area.

Large contrasts in the stress fields and seismicity depth are observed across the junction between the SAF and SJFZ near Cajon Pass. To the northwest of the junction in the San Gabriel Mountains the dominant stress field is transpressional (R~0.9), while to the southeast, the dominant stress field is transtensional (R~0.2) and the average S_{Hmax} direction rotates more than 15º. The seismogenic depth varies by ~7 km from northwest to southeast of the SAF and SJFZ junction. These variations occur over a distance less than 20 km, implying strong effects of fault properties on the stress field and the importance of high-resolution analysis of the stress field of the type done in this study.

Results of stress ratios inverted from the background seismicity in 5 separate time intervals of ~8 years between 1981 and 2017 are overall consistent with the discussed stress ratio variations for the combined 1981 and 2017 data, showing compressional stress components near high topography and tensional stress components near CH. The time interval 1986-1993 produces the largest transpressional stress components near the SGP area, where two transpressional events with magnitudes M_w 5.6 and 5.0 occurred in 1986 and 1988 (Figure S2).

Earthquake ruptures produce rock damage in their source volume (e.g., Lyakhovsky et al., 1997; Lockner et al., 1992; Aben et al., 2019). The evolution of rock damage can modify the properties and dynamics of fault zones on a geological time scale (e.g., Ben-Zion and Sammis, 2003). Estimated rock damage production by ongoing background seismicity in Southern California shows several prominent damage zones (Ben-Zion and Zaliapin, 2019). The SJFZ and the SCTR, especially near major fault junctions (CP and SGP), are among the regions with the highest relative damage production, and the seismicity and rock damage become more pronounced and continuous with depth. The depth ranges with high concentration of seismicity and rock damage near CH, SGP, and CP areas are consistent with the depth range of the highest transpressional and transtensional stress components.

The Moho has significant depth variations below the SCTR (Zhu and Kanamori, 2000; Ozakin and Ben-Zion 2015) and several studies discussed the association of Moho depth changes with enhanced generation of rock damage and reduced ability of faults to localize in the upper brittle crust (Lyakhovsky and Ben-Zion, 2009; Zaliapin and Ben-Zion, 2019). Earthquakes in such areas are expected to be distributed in space and exhibit a high diversity of mechanisms as observed near the SCTR. All three faulting types (strike-slip, reverse and normal) estimated from focal mechanisms of the declustered events exist in the entire SCTR, with increased number of normal and reverse faulting around CH and CP areas, respectively (Figure S3). The dip-slip events near the SCTR comprise a smaller fraction of the background seismicity than the strike-slip events and have mostly $M_w < 3.5$. The relatively small magnitudes of the dip-slip events suggest that they are mainly associated with off-fault damage zones rather than the main strike-slip plate-boundary faults. Another manifestation of complexity in the SCTR is that strike

angles of the declustered focal mechanisms are distributed in a range of directions (Figure S3) with no clear relationship between the strike angles and faulting types.

Additional insights on dominant loading mechanisms and crustal stress parameters in different areas can be obtained by comparing the stress inversion results with surface strain-rate from geodetic data in regions with/out topography and with/out inferred deep creep (e.g. Townend and Zoback, 2006). Deriving focal mechanisms for smaller events will allow stress inversions to be done using smaller sub-volumes and time intervals, leading to better resolution of stress variations in space and time. Numerical simulations of stress/strain evolution in crustal models with different loadings, different fault geometries, and different in viscoelastic structures can aid the interpretation of results. These studies will be the attempted in future work.

6. Acknowledgments

The earthquake and focal mechanism catalogs used in the paper are available in the Southern California Earthquake Data Center (https://scedc.caltech.edu/). The study was supported by the Southern California Earthquake Center (based on NSF Cooperative Agreement EAR-1600087 and USGS Cooperative Agreement G17AC00047) and the U.S. Department of Energy (award DE-SC0016520).. PMG acknowledges funding from the Helmholtz Association in the frame of the Young Investigators Group VH-NG-1232 (SAIDAN).

7. References

Aben, F. M., Brantut, N., Mitchell, T. M., & David, E. C. (2019). Rupture energetics in crustal rock from laboratory-scale seismic tomography. *Geophysical Research Letters*, *46*(13), 7337-7344.

Abolfathian, N., Martínez-Garzón, P., & Ben-Zion, Y. (2019). Spatiotemporal variations of stress and strain parameters in the San Jacinto fault zone. *Pure and Applied Geophysics*, *176*(3), 1145-1168.

Ben-Zion, Y., & Sammis, C. G. (2003). Characterization of fault zones. *Pure and Applied Geophysics*, *160*(3-4), 677-715.

Ben-Zion, Y., & Zaliapin, I. (2019). Spatial variations of rock damage production by earthquakes in southern California. *Earth and Planetary Science Letters*, *512*, 184-193.

Bott, M. H. P. (1959). The mechanics of oblique slip faulting. *Geological Magazine*, *96*(02), 109-117.

Cooke, M. L., & Beyer, J. L. (2018). Off-Fault Focal Mechanisms Not Representative of Interseismic Fault Loading Suggest Deep Creep on the Northern San Jacinto Fault. *Geophysical Research Letters*, *45*(17), 8976-8984.

Fialko, Y., Rivera, L., & Kanamori, H. (2005). Estimate of differential stress in the upper crust from variations in topography and strike along the San Andreas fault. Geophysical Journal International, 160(2), 527–532.

Fuis, G. S., Scheirer, D. S., Langenheim, V. E., & Kohler, M. D. (2012). A new perspective on the geometry of the San Andreas fault in southern California and its relationship to lithospheric structure. *Bulletin of the Seismological Society of America*, *102*(1), 236-251.

Hardebeck, J. L. (2014). The impact of static stress change, dynamic stress change, and the background stress on aftershock focal mechanisms. *Journal of Geophysical Research: Solid Earth*, *119*(11), 8239-8266.

Hardebeck, J. L., & Hauksson, E. (2001). Crustal stress field in southern California and its implications for fault mechanics. *Journal of Geophysical Research: Solid Earth*, *106*(B10), 21859-21882.

Hardebeck, J. L., & Michael, A. J. (2006). Damped regional-scale stress inversions: Methodology and examples for southern California and the Coalinga aftershock sequence. *Journal of Geophysical Research: Solid Earth*, *111*(B11).

Hartigan, J. A., & Wong, M. A. (1979). Algorithm AS 136: A k-means clustering algorithm. *Journal of the Royal Statistical Society. Series C (Applied Statistics)*, *28*(1), 100-108.

Hauksson, E., Yang, W., & Shearer, P. M. (2012). Waveform relocated earthquake catalog for southern California (1981 to June 2011). *Bulletin of the Seismological Society of America*, *102*(5), 2239-2244.

Lockner, D. A., Byerlee, J. D., Kuksenko, V., Ponomarev, A., & Sidorin, A. (1992). Observations of quasistatic fault growth from acoustic emissions. In *International Geophysics* (Vol. 51, pp. 3-31). Academic Press.

Lund, B., & Townend, J. (2007). Calculating horizontal stress orientations with full or partial knowledge of the tectonic stress tensor. *Geophysical Journal International*, *170*(3), 1328-1335.

Lyakhovsky, V., & Ben-Zion, Y. (2009). Evolving geometrical and material properties of fault zones in a damage rheology model. *Geochemistry, Geophysics, Geosystems*, *10*(11), Q11011.

Lyakhovsky, V., Ben-Zion, Y., & Agnon, A. (1997). Distributed damage, faulting, and friction. *Journal of Geophysical Research: Solid Earth*, *102*(B12), 27635-27649.

Martínez-Garzón, P., Ben-Zion, Y., Abolfathian, N., Kwiatek, G., & Bohnhoff, M. (2016a). A refined methodology for stress inversions of earthquake focal mechanisms. *J. Geophys. Res*., 121, 8666-8687.

Martínez-Garzón, P., Kwiatek, G., Bohnhoff, M., & Dresen, G. (2016b). Impact of fluid injection on fracture reactivation at The Geysers geothermal field. Journal of Geophysical Research: Solid Earth, 121(10), 7432-7449.

Martínez-Garzón, P., Kwiatek, G., Ickrath, M., & Bohnhoff, M. (2014). MSATSI: A MATLAB package for stress inversion combining solid classic methodology, a new simplified user-handling, and a visualization tool. *Seismological Research Letters*, *85*(4), 896-904.

Matti, J. C., Morton, D. M., & Powell, R. E. (1993). Paleogeographic evolution of the San Andreas fault in southern California: A reconstruction based on a new cross-fault correlation. *The San Andreas fault system: Displacement, palinspastic reconstruction, and geologic evolution*, *178*, 107-159.

McCloskey, J., Nalbant, S. S., Steacy, S., Nostro, C., Scotti, O., & Baumont, D. (2003). Structural constraints on the spatial distribution of aftershocks. *Geophysical research letters*, *30*(12).

McKenzie, D. P. (1969). The relation between fault plane solutions for earthquakes and the directions of the principal stresses. *Bulletin of the Seismological Society of America*, *59*(2), 591-601.

Michael, A. J. (1984). Determination of stress from slip data: faults and folds. *Journal of Geophysical Research: Solid Earth*, *89*(B13), 11517-11526.

Michael, A. J. (1987). Use of focal mechanisms to determine stress: a control study. *Journal of Geophysical Research: Solid Earth*, *92*(B1), 357-368.

Ozakin, Y., & Ben-Zion, Y. (2015). Systematic receiver function analysis of the Moho geometry in the Southern California Plate-Boundary region. *Pure and Applied Geophysics*, *172*(5), 1167-1184.

Spotila, J. A., Farley, K. A., Yule, J. D., & Reiners, P. W. (2001). Near‐field transpressive deformation along the San Andreas fault zone in southern California, based on exhumation constrained by (U‐Th)/He dating. *Journal of Geophysical Research: Solid Earth*, *106*(B12), 30909-30922.

Townend, J., & Zoback, M. D. (2006). Stress, strain, and mountain building in central Japan. *Journal of Geophysical Research: Solid Earth*, *111*(B3).

Vavryčuk, V. (2011). Principal earthquakes: Theory and observations from the 2008 West Bohemia swarm. *Earth and Planetary Science Letters*, *305*(3-4), 290-296.

Vavryčuk, V. (2014). Iterative joint inversion for stress and fault orientations from focal mechanisms. *Geophysical Journal International*, *199*(1), 69-77.

Wallace, R. E. (1951). Geometry of shearing stress and relation to faulting. *The journal of Geology*, *59*(2), 118-130.

Wdowinski, S. (2009). Deep creep as a cause for the excess seismicity along the San Jacinto fault. Nature Geoscience, 2(12), 882–885.

Yang, W., & Hauksson, E. (2013). The tectonic crustal stress field and style of faulting along the Pacific North America Plate boundary in Southern California. *Geophysical Journal International*, *194*(1), 100-117.

Yang, W., Hauksson, E., & Shearer, P. M. (2012). Computing a large refined catalog of focal mechanisms for southern California (1981–2010): Temporal stability of the style of faulting. *Bulletin of the Seismological Society of America*, *102*(3), 1179-1194.

552 Yule, D., & Sieh, K. (2003). Complexities of the San Andreas fault near San
553 Gorgonio Pass: Implications for large earthquakes. *Journal of Geophysical Research:*
554 *Solid Earth*, *108*(B11).
555 Zaliapin, I., & Ben-Zion, Y. (2013). Earthquake clusters in southern California I:
556 Identification and stability. *Journal of Geophysical Research: Solid Earth*, *118*(6), 2847-
557 2864.
558 Zaliapin, I., & Ben-Zion, Y. (2020). Earthquake declustering using the nearest-
559 neighbor approach in space-time-magnitude domain, *Journal of Geophysical Research*,
560 doi: 10.1029/2018JB017120.
561 Zoback, M. L. (1992). First- and second-order patterns of stress in the lithosphere:
562 The World Stress Map Project. *Journal of Geophysical Research: Solid Earth*, *97*(B8),
563 11703-11728.
564 Zhu, L., & Kanamori, H. (2000). Moho depth variation in southern California
565 from teleseismic receiver functions. *Journal of Geophysical Research: Solid*
566 *Earth*, *105*(B2), 2969-2980.

Table 1. Seismic statistics in SCTR, comparing foreshocks, mainshocks, and aftershocks.

1981 to 2017 -1 to 30 km depth	No. of events	No. of events %	Seismogenic thickness (90%)	Maximum Magnitude (90%)	Mean Magnitude	Median Magnitude
Foreshock	2,128	14.2	16.8	2.63	2.28	2.21
Mainshock	3,218	21.5	16.9	3.12	2.51	2.37
AfterShock	9,648	64.3	13.5	2.94	2.42	2.3

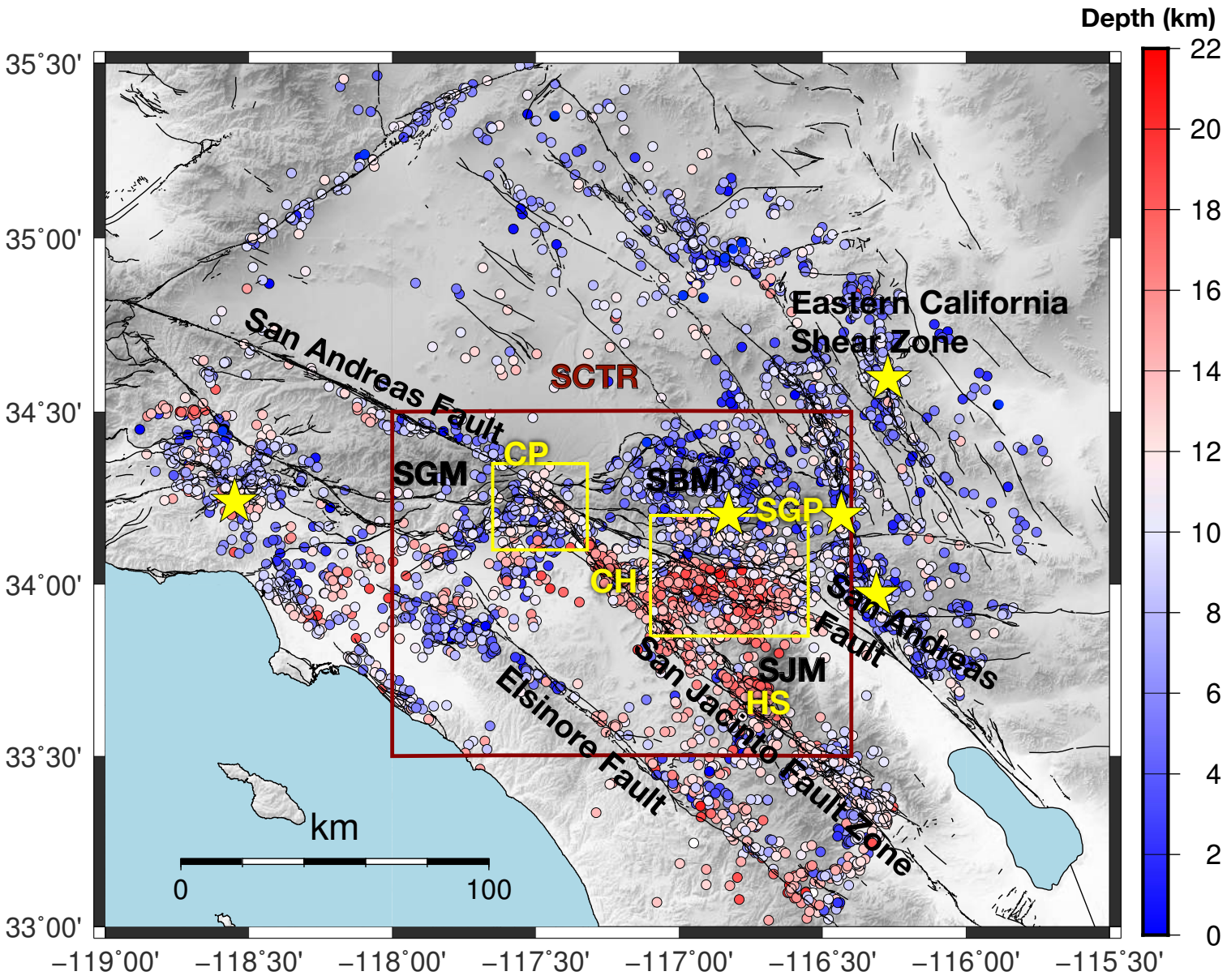

Figure 1. Distribution of declustered seismicity with focal mechanisms in the selected region in Southern California, between 1981 to 2017 used for the stress inversion. Each event is color-coded with its hypocentral depth. The brown rectangle denotes a selected region around the South Central Transverse Ranges (SCTR). The yellow squares show focused regions of study, Cajon Pass (CP), and San Gorgonio Pass (SGP). Faults are marked in black lines. Stars show events larger than magnitude 6 in the region during the selected time period. SCTR and yellow fonts in the figure shows regions of study, while black fonts defines geology of the area. (SGM: San Gabriel Mountains; SBM: San Bernardino Mountains; SJM: San Jacinto Mountains; CH: Crafton Hills; HS: Hot Springs).

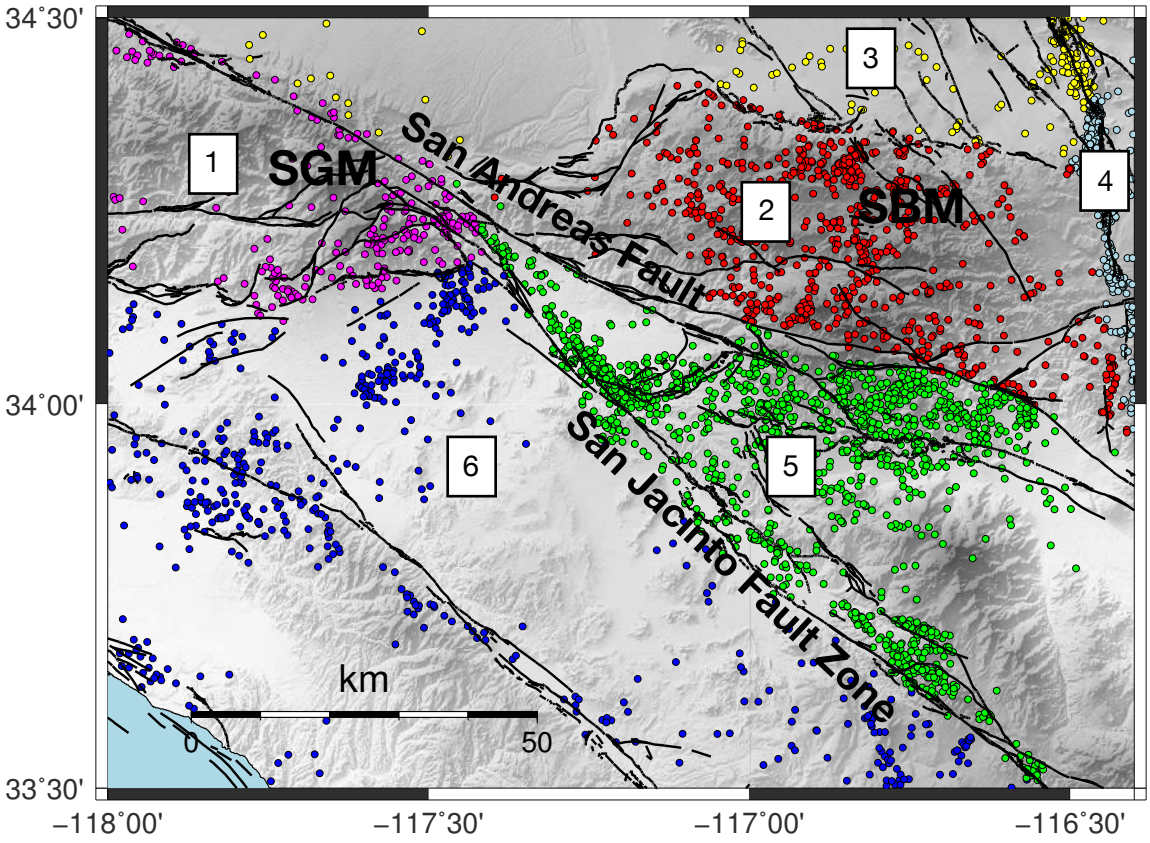

Figure 2. Seismicity distribution in six subregions in the selected region around the South Central Transverse Ranges: (1) San Gabriel Mountains (SGM) in purple, (2) San Bernardino Mountains (SBM) in red, (3) northern part in yellow, (4) eastern section of the SBM in cyan, (5) between the San Andreas Fault (SAF) and San Jacinto Fault Zone (SJFZ) in green, (6) western section of the SJFZ in blue.

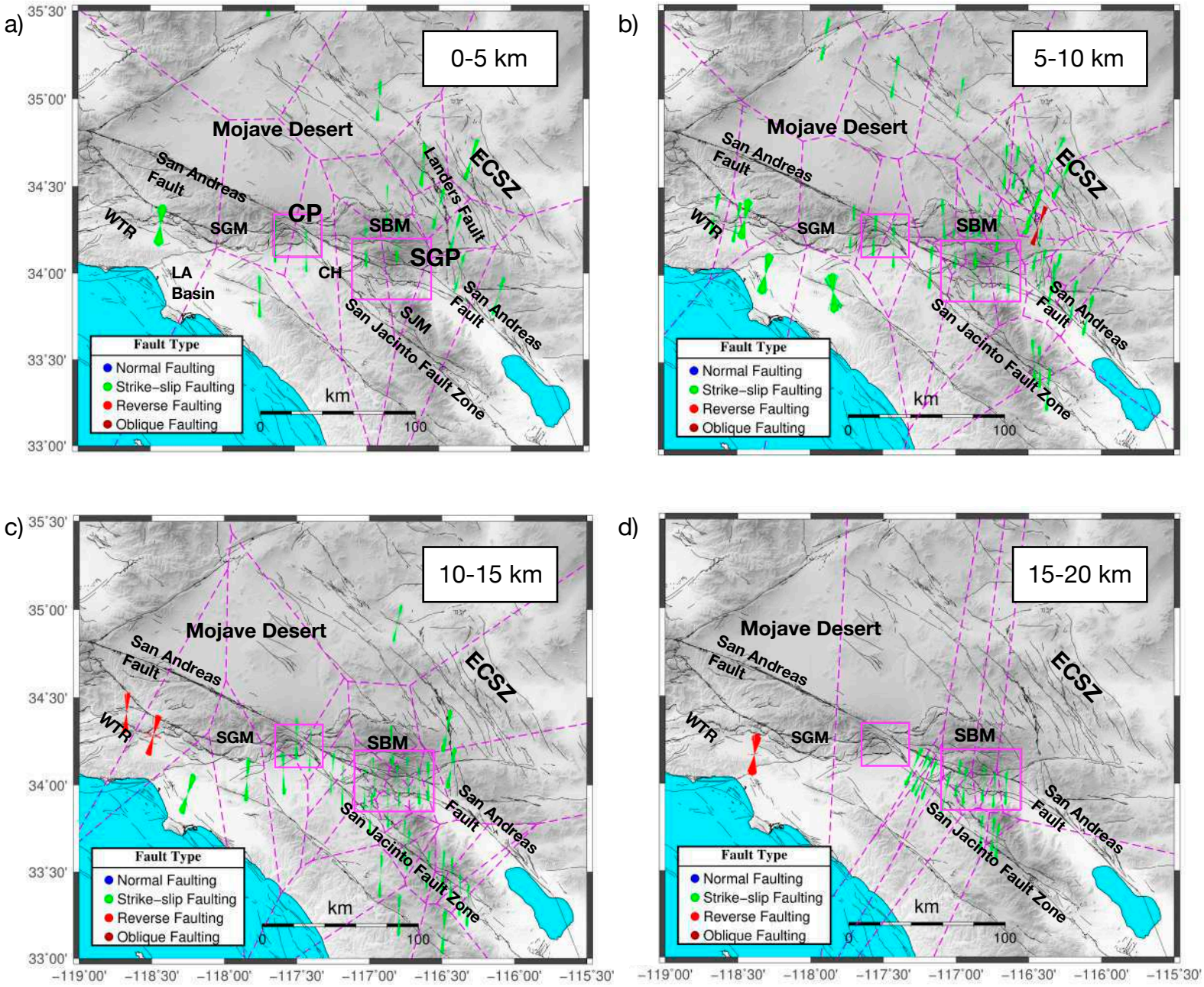

Figure 3. Regional distribution of the maximum horizontal compressional stress orientations (S_{Hmax}) at (a) 0 to 5 km, (b) 5 to 10 km, (c) 10 to 15 km, (d) 15 to 20 km depth sections. The variations in S_{Hmax} orientations show the uncertainty of 95% confidence interval. The orientations are color-coded in red, green, blue, and brown denoting reverse, strike-slip, normal and oblique faulting, respectively. Purple dashed lines indicate the used Voronoi cells. WTR: West Transverse Ranges; SGM: San Gabriel Mountains; CP: Cajon Pass; CH: Crafton Hills; SJM: San Jacinto Mountains; SGP: San Gorgonio Pass; SBM: San Bernardino Mountains; ECSZ: Eastern California Shear Zone.

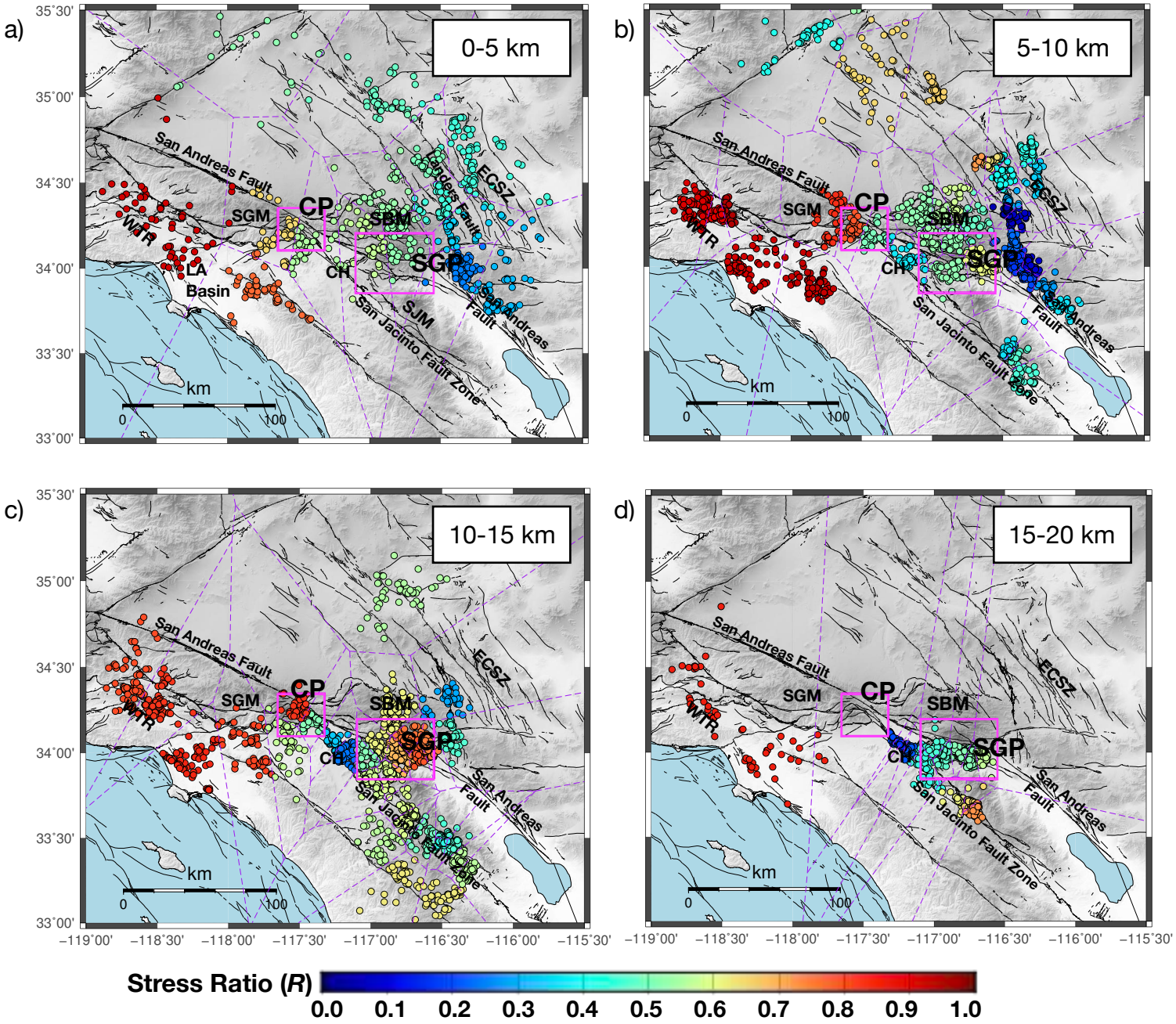

Figure 4. Regional seismicity distribution color-coded with values of the stress ratio *R* at (a) 0 to 5 km, (b) 5 to 10 km, (c) 10 to 15 km, (d) 15 to 20 km depth sections. In a strike-slip faulting environment, *R*-values around 0.5, 0 and 1 indicate pure strike-slip, transtensional and transpressional stress regimes, respectively. Purple dashed lines indicate the used Voronoi cells.

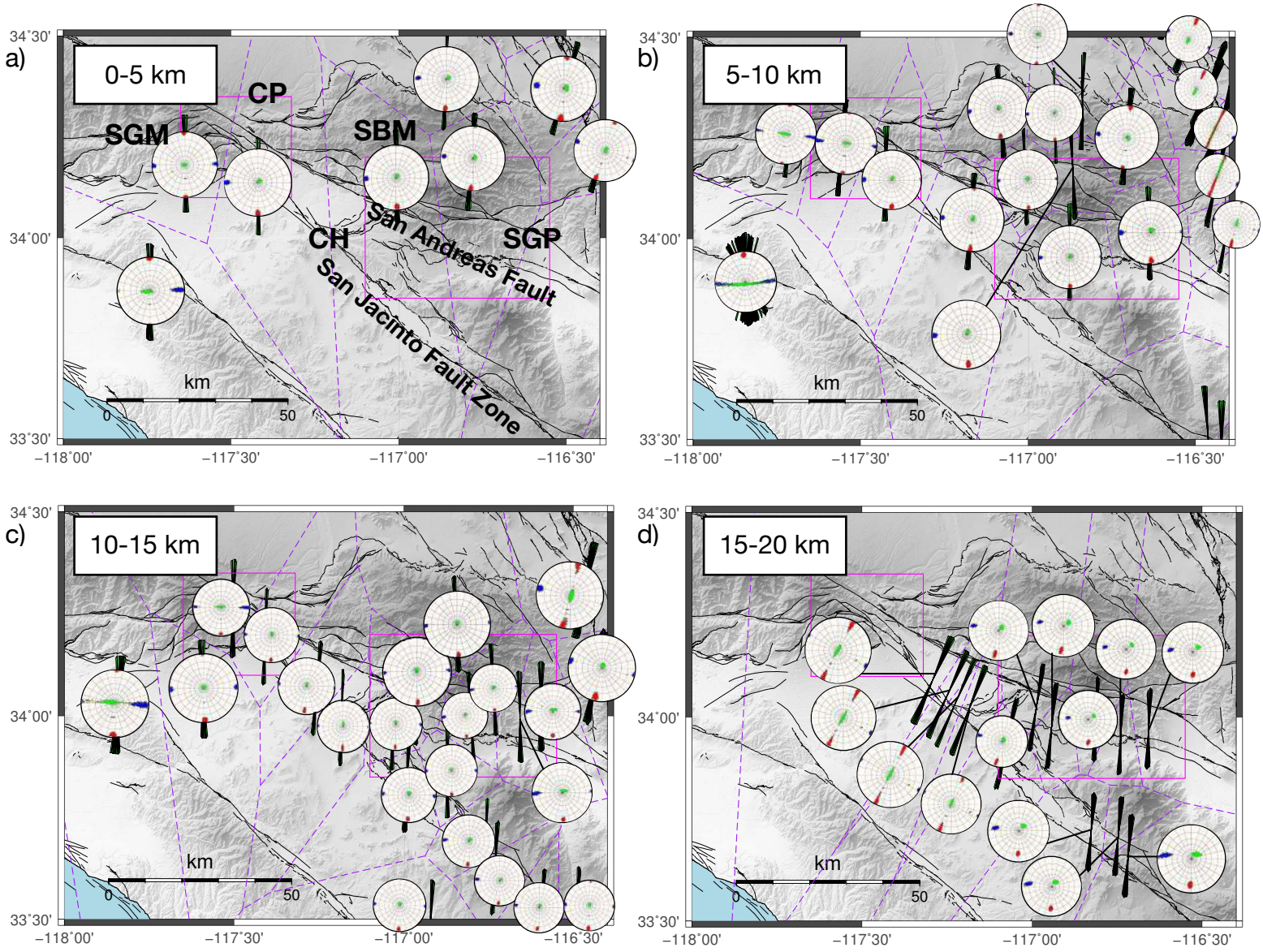

Figure 5. Distribution of the maximum horizontal compressional stress orientations (S_{Hmax}) in fan symbols and the principal stress orientations (Stereonets) in the selected region around SCTR at (a) 0 to 5 km, (b) 5 to 10 km, (c) 10 to 15 km, (d) 15 to 20 km depth sections. The variations in S_{Hmax} orientations show the uncertainty of 95% confidence interval. The maximum, intermediate and minimum principal stresses in the stereonets are indicated with red, green, and blue, respectively. Purple dashed lines indicate the used Voronoi cells. CP and SGP shown in pink rectangles.

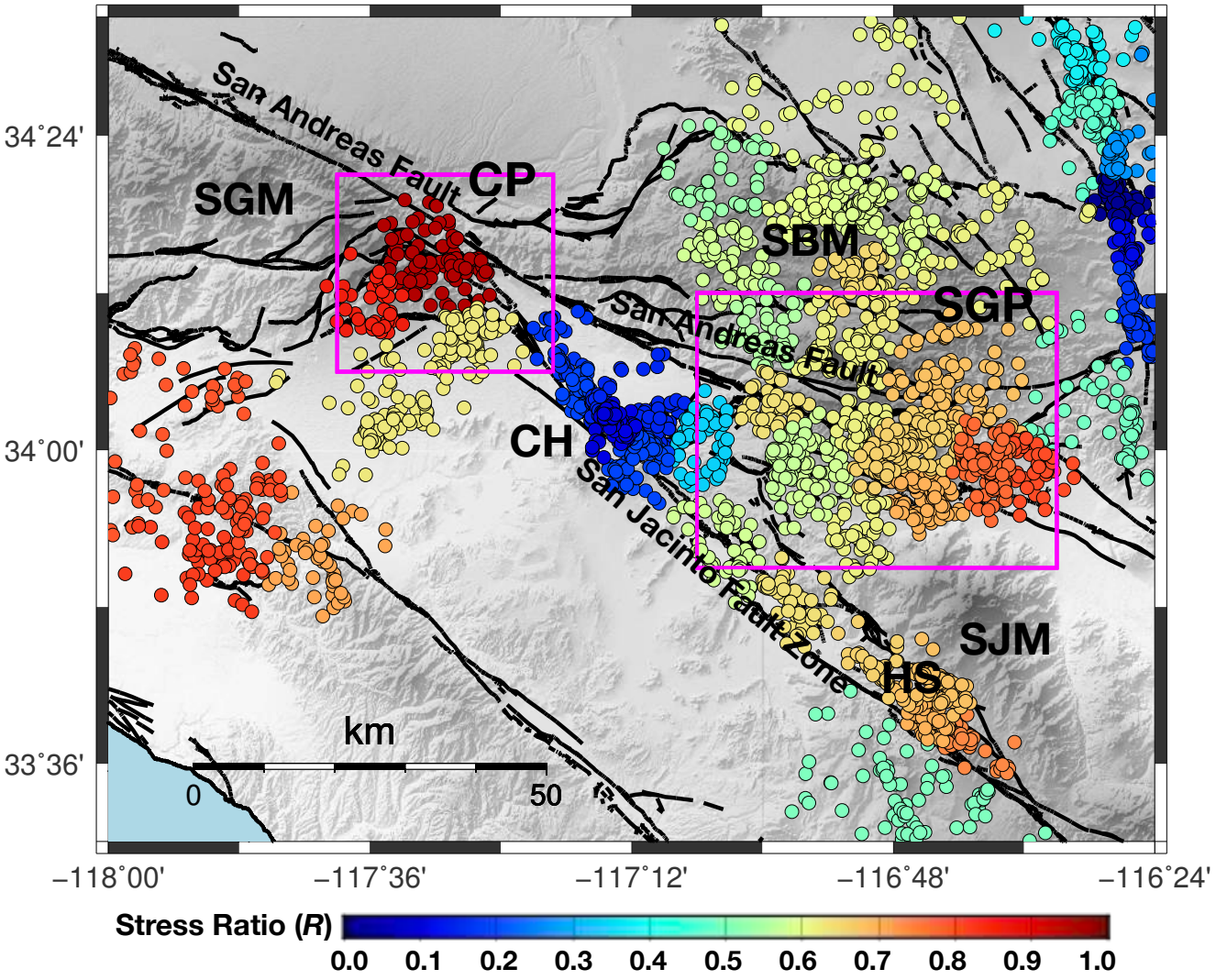

Figure 6. Seismicity color-coded with values of the stress ratio *R* in the selected region around SCTR. Background seismicity distributed in 6 sections based on figure 2. Signs are as in figures 4.

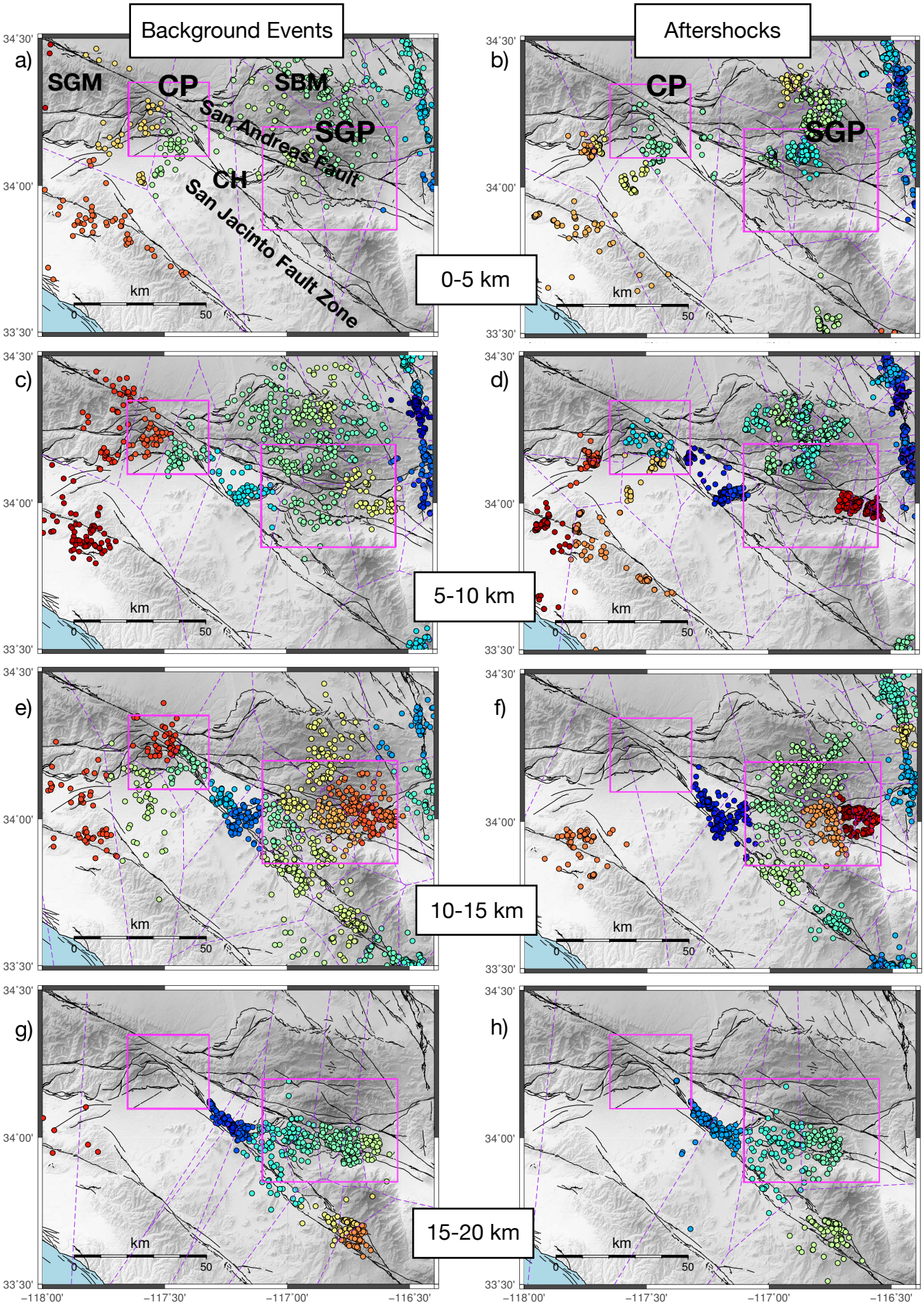
Background Events
Aftershocks
a)
b)
c)
d)
e)
f)
g)
h)
SGM
CP
SBM
SGP
CH
San Andreas Fault
San Jacinto Fault Zone
0-5 km
5-10 km
10-15 km
15-20 km
km
0
50
34°30'
34°00'
33°30'
−118°00'
−117°30'
−117°00'
−116°30'
Stress Ratio (R)
0.0 0.1 0.2 0.3 0.4 0.5 0.6 0.7 0.8 0.9 1.0

Figure 7. Seismicity color-coded with values of the stress ratio *R,* at (a,b) 0 to 5 km, (c,d) 5 to 10 km, (e,f) 10 to 15 km, (g,h) 15 to 20 km depth sections. Subplots (a,c,e,g) show the variation of the stress ratio regarding to the mainshocks while (b,d,f,h) are estimated inverting the aftershock events. Signs are as in figures 4.

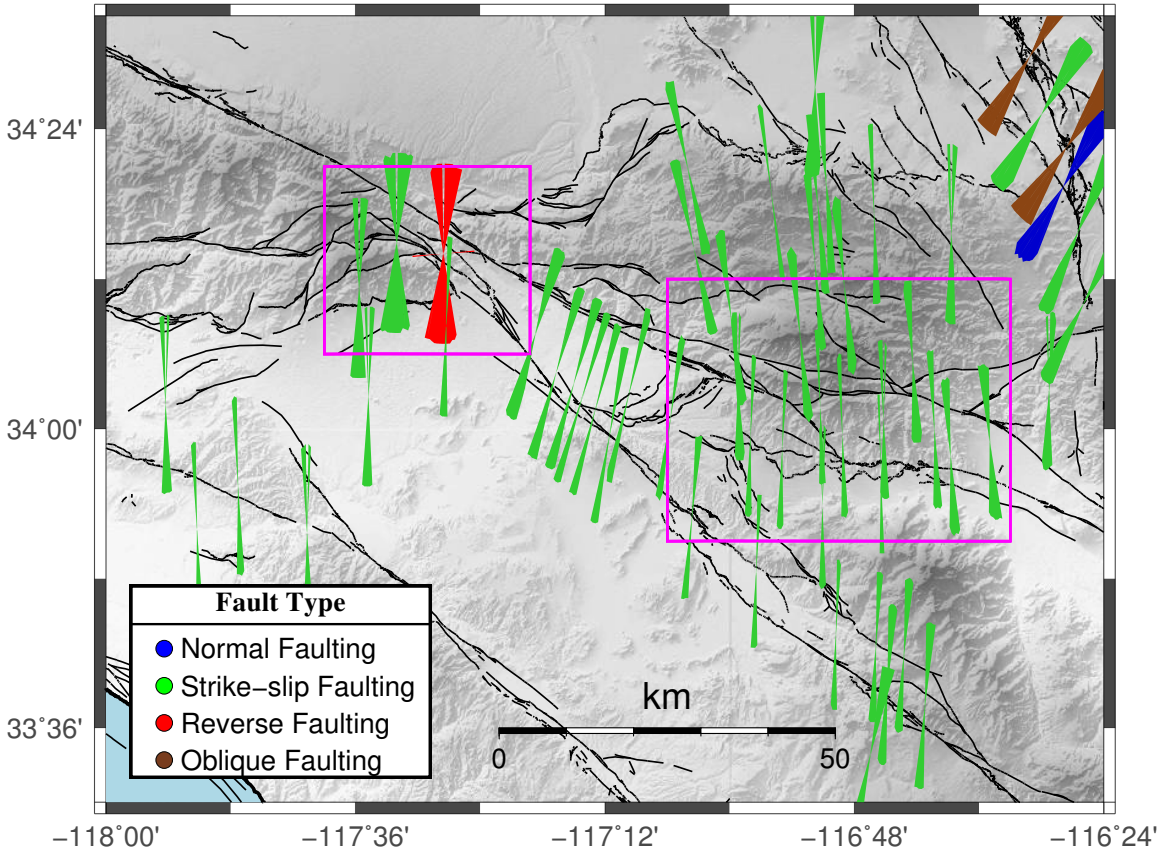

Figure S1. Distribution of the maximum horizontal compressional stress orientations (S_{Hmax}) in the selected region around SCTR based on data distribution in six subregions as in Figure 2. Signs are as in Figure 3.

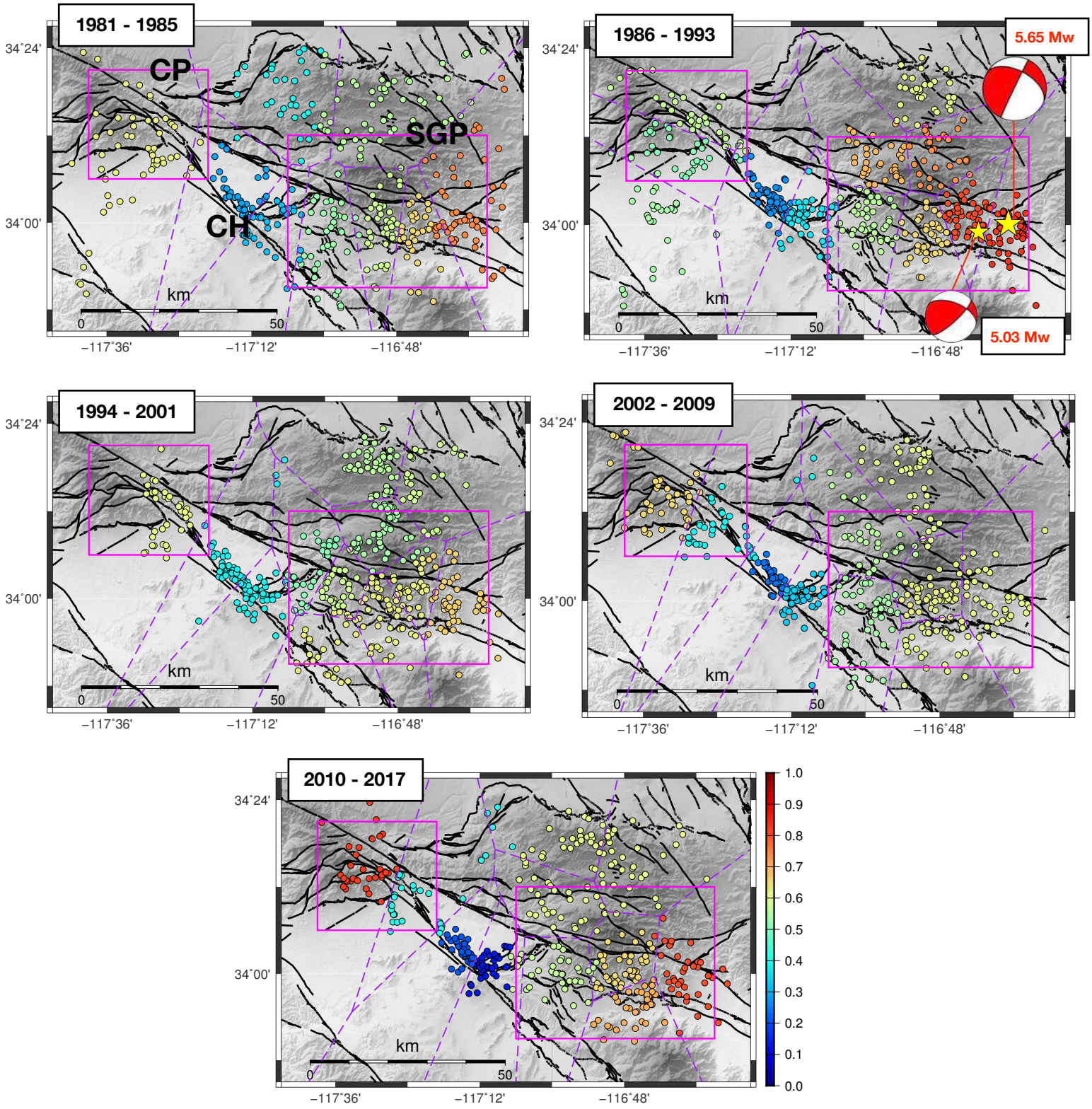

Figure S2. Temporal Variations of stress ratios near CP and SGP. Signs are as in Figure 4.

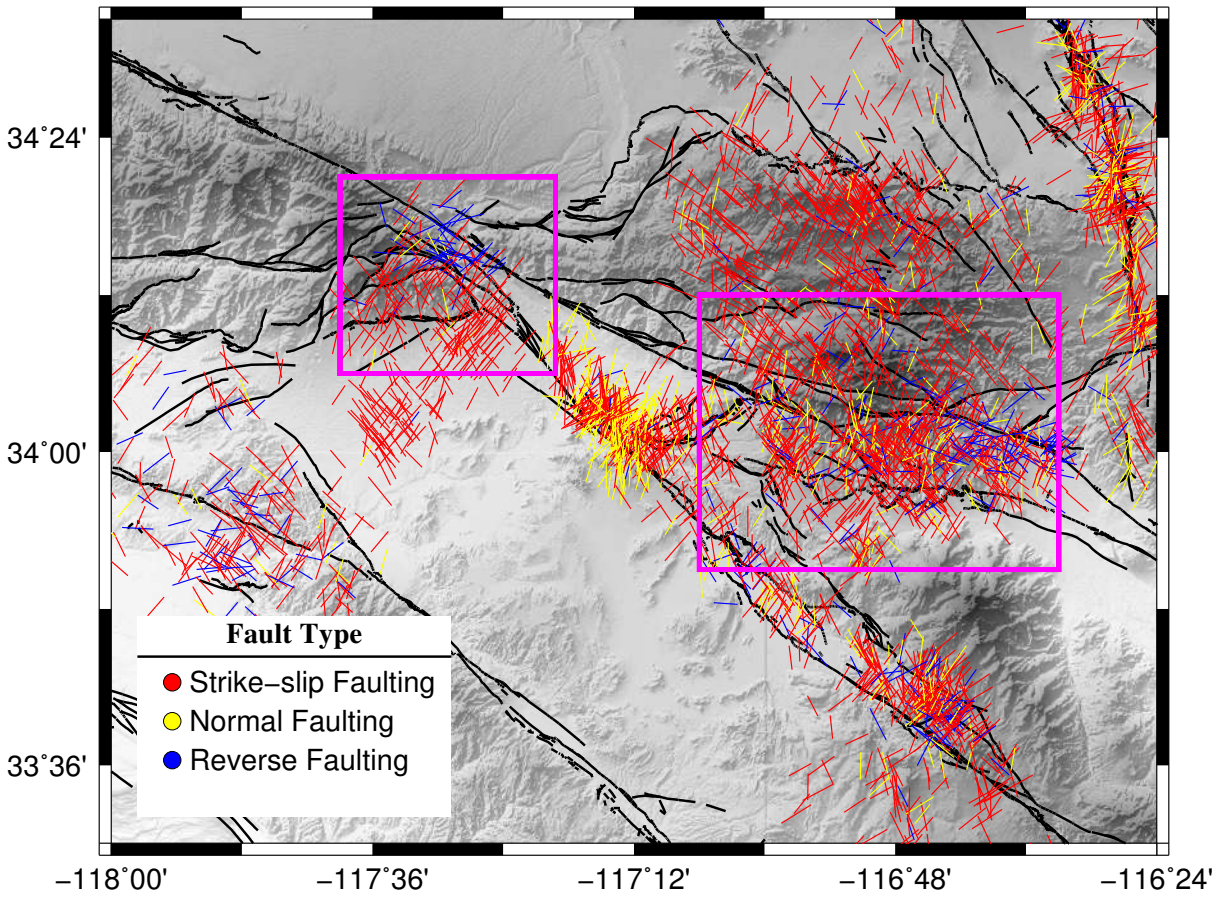

Figure S3. Distribution of the strike angles of the focal mechanisms from the declustered catalog, color-coded with the main types of faulting in the selected region around SCTR based on data distribution in six subregions as in Figure 2.